Korean J. Chem. Eng., 39(11), 3083-3091 (2022)
DOI: 10.1007/s11814-022-1147-7

pISSN: 0256-1115
eISSN: 1975-7220

Synthesis of manganese-iron oxides/activated carbon as a highly effective adsorbent for sulfamerazine pollutant removal

Wenxiu Zhu*,,‡, Xinghao Liu*,**,‡, Zhaoguang Yang*,**,†, and Haipu Li*,**,†**

*Center for Environment and Water Resource, College of Chemistry and Chemical Engineering, Central South University, Changsha 410083, P. R. China
**Key Laboratory of Hunan Province for Water Environment and Agriculture Product Safety, Changsha 410083, P. R. China

(*Received 19 January 2022 • Revised 28 March 2022 • Accepted 14 April 2022*)

Abstract−Considering the frequent detection in environment and the potential threat to human health and ecoenvironment, achieving removal of sulfamerazine (SMZ) from the aquatic environment is of great significance. In this study, the magnetically separable manganese-iron oxides/activated carbon (Mn-Fe_3O_4/AC) was synthesized by simple co-precipitation method and was used to remove SMZ from solution. Doping manganese oxide could change the specific surface areas of the prepared materials, thus providing more active sites for adsorption and improving the adsorption capacity of Mn-Fe_3O_4/AC for SMZ (maximum adsorption capacity 146 mg g^{-1}). The kinetic and thermodynamic study showed that the adsorption of SMZ on Mn-Fe_3O_4/AC was endothermic and spontaneous, and followed the pseudo-second-order kinetics model and Langmuir model. Efficient removal of SMZ was attributed to varieties of non-covalent interactions between it and Mn-Fe_3O_4/AC, including electrostatic interactions, hydrogen bonds and π-π electron donor-acceptor interactions. In addition, SMZ could be degraded by oxidation via redox reactions. After six cycles of use, Mn-Fe_3O_4/AC still had good adsorption capability.

Keywords: SMZ, AC, Doping Manganese, Adsorption Mechanism

INTRODUCTION

Antibiotics play important roles in preventing bacterial infection in animals and humans [1]. However, the abuse of antibiotics can raise antimicrobial resistance in bacterial pathogens, which has caused concern around the globe [2]. Sulfamerazine (SMZ), as one kind of common sulfa-antibiotic, is used for animal husbandry and disease treatment because of its effective therapeutic properties and low price [3,4]. Now, it has been detected in the water environment with the concentration ranging from 0.19 to 126 mg L^{-1} [5]. If existing in environment for a long time, it can pose a serious threat to human health and the ecosystem [3].

Adsorption is one of available techniques for removal of antibiotics, because of its excellent advantages, including low cost, high efficiency, easy operation, and wide adaptability. Activated carbon (AC) as a classic adsorbent is often used to remove odors, pigment, antibiotics, and other pollutants [6]. However, it is difficult to separate and regenerate, which limits its application. Many researchers made AC impart magnetic properties, which not only accomplished rapid separation from solution, but also enhanced adsorption capacity [7]. For example, Yu et al. reported glyphosate maximum adsorption capacity of prepared magnetic AC was approximately 2.8 times higher than that of raw AC [8]. Although the problem of difficult recovery of adsorbent from solution has been solved, the adsorption capacity of magnetic AC still needs to be increased [9].

Transition metals and/or their oxides doped in iron oxide can significantly improve the characteristics, including stability, catalytic activity, and adsorption capacity [10-12]. Manganese oxide is a great choice as significant scavenger of various heavy metals and/or organic pollutants, such as Cr [13], tetracycline [14], and methylene blue [15]. In addition, Fe-containing adsorbents doped with manganese oxide are more active than the adsorbents without manganese oxide [11]. Because the doping of manganese oxide not only prevents agglomeration of iron oxides to increase available adsorption specific surface area, but also increases the redox capability of composite materials [16,17]. For example, Cholhwan et al. synthesized a citric acid modified core-shell magnetic manganese dioxide with high adsorption capacity for basic dyes in a relatively short time compared to other adsorbents [15]. Furthermore, magnetic manganese oxide has certain redox properties due to the multivalent state of manganese. For example, Zhang et al. reported that Fe_3O_4-MnO_2 can significantly promote the decomposition of ozone to generate hydroxyl radicals (•OH), and bisphenol A degradation ratio in Fe_3O_4-MnO_2/O_3 system was higher than that in ozonation system [18]. As known, a catalytic reaction mainly occurs at the gas-solid-liquid interface; therefore, the adsorption of reactants on the solid catalyst is an indispensable step [19]. However, the adsorption mechanism on solid catalysts still needs further exploration.

This study was committed to developing efficient and promising manganese-doped activated carbon-based magnetic adsorbent (Mn-Fe_3O_4/AC), which was prepared via simple co-precipitation

†To whom correspondence should be addressed.
E-mail: zgyang@csu.edu.cn, lihaipu@csu.edu.cn
‡The first two authors contributed equally to this study.

method. And the adsorption performance of Mn-Fe_3O_4/AC for SMZ removal was studied via kinetic and thermodynamic models. Furthermore, the adsorption characteristics and mechanism were discussed.

MATERIAL AND METHODS

1. Materials and Preparation Materials

The powder AC was obtained from Tianjin Ding Shengxin Chemical Co. Ltd. (200 mesh, Tianjin, China). Ferric chloride ($FeCl_3$), ferrous sulfate heptahydrate ($FeSO_4 \cdot 7H_2O$), and manganese chloride tetrahydrate ($MnCl_2 \cdot 4H_2O$) were obtained from Shanghai Hushi Co. Ltd. (Shanghai, China). SMZ (purity: 99.99%) was purchased from National Institute for Drug Control (Beijing, China). High performance liquid chromatography (HPLC) grade methanol (MeOH) and formic acid (FA) were purchased from Fisher Scientific, Belgium. And the chemical reagents were analytical grade unless otherwise specified and used without further purification. Ultra-pure water (UP-water, 18.25 MΩ·cm) was used in whole experiments.

The AC was cleaned with 0.1 mol L^{-1} HNO_3, washed with UP-water to neutral and then dried for later use. The preparation process of Mn-Fe_3O_4/AC is shown in Fig. S1 in Supplementary materials. $FeCl_3$ (4.56 g), $FeSO_4 \cdot 7H_2O$ (3.90 g), specified amount of $MnCl_2 \cdot 4H_2O$ (molar ratio Fe^{2+} : Mn^{2+}=1 : 10, 1 : 5, and 1 : 1) and acidified AC (3.25 g) were added into three-necked flask with 40 mL UP-water. After the suspension was heated to 343 K in water bath, the 50 mL 5 mol L^{-1} NaOH solution was added dropwise into the suspension. After aging for 2 h, the obtained solid was washed with UP-water to neutral and dried in oven at 378 K. Finally, the dried solid was annealed with heating rate of 276 K min^{-1} to 873 K for 5 h to get Mn-Fe_3O_4/AC-10, Mn-Fe_3O_4/AC-5, and Mn-Fe_3O_4/AC-1. Fe_3O_4/AC was obtained as the above method without $MnCl_2 \cdot 4H_2O$.

2. Characterization

The surface morphology of prepared materials was characterized by scanning electron microscopy (SEM, Zeiss Sigma 300, Germany) coupled with energy dispersive spectrometer (EDS). The crystal phases of all samples were determined by X-ray diffraction (XRD, Bruker D8 advance, Germany) using Cu Kα radiation with Bragg angle 10-90°. The surface functional groups of samples were confirmed by Fourier transform infrared spectroscopy (FTIR, Thermo Fisher Scientific, USA) and X-ray photoelectron spectroscopy (XPS, EscaLab Xi^+, USA). The Brunauer-Emmett-Teller (BET) surface area measurement was performed on an ASAP 2460 surface area analyzer, which came from USA. The zero charge potential of materials was detected by Nano SZ-100 (Horiba, France).

3. Adsorption Experiments and Analytical Method

The adsorption capacities of prepared materials, including AC, Fe_3O_4/AC, and Mn-Fe_3O_4/AC, were investigated by batch experiments, and adjusting pH by negligible volume of 0.1 mol L^{-1} or 0.01 mol L^{-1} HCl and/or NaOH in solution. Then the conical flasks were put into shakers with speed of 120 rpm for 48 h to achieve adsorption equilibrium. The Mn-Fe_3O_4/AC was highly uniformly dispersed in solution, and it could be easily separated by magnet (Fig. S2). Before obtained samples entered analytical instrument, they were filtered by 0.22 μm membrane. The residual SMZ in solution was detected by HPLC with ZORBAX SB-C18 (5 μm, 4.6× 250 mm, Agilent 1260, USA). MeOH and UP-water with 0.1% FA (40 : 60 (v/v)) were used as mobile phases at a flow rate of 1.0 mL min^{-1} and the detection wavelength was 265 nm.

The removal efficiencies and the adsorption capacities of adsorbents are calculated via the following equations (Eqs: (1-3)):

$$\eta\% = \frac{C_0 - C_t}{C_0} \times 100\% \quad (1)$$

$$q_e = \frac{(C_0 - C_e) \times V}{m} \quad (2)$$

$$q_t = \frac{(C_0 - C_t) \times V}{m} \quad (3)$$

where η is the removal efficiency of SMZ; C_0 (mg L^{-1}) and C_t are the concentration of SMZ initially and at any time t, respectively; C_e (mg L^{-1}) is the concentration of adsorption equilibrium; q_t (mg g^{-1}) is instantaneous adsorption capacity; q_e (mg g^{-1}) is equilibrium adsorption capacity; m (g) is the mass of the adsorbent, and V (L) is the volume of solution. All of the experimental data were the averages of triplicate determinations, and the relative errors of the date were less than 5%.

RESULTS AND DISCUSSION

1. Targeted Composite Material Confirmation

Fig. 1 showed the morphology of the prepared samples. The acidified AC sample had a smooth surface and fewer holes (Fig. 1(a)). After Fe_3O_4 and/or manganese oxides were doped in AC, the structures became luxuriantly porous (Fig. 1(b)-(c)). The results of EDS element mapping including the Mn (Fig. 1(e)) and Fe (Fig. 1(f)) further confirmed that the iron-manganese oxides could be evenly distributed on the surface of AC. In addition, the proportion of Fe/Mn was about 11.2, which was close to the ratio of the preset prepared material (Mn-Fe_3O_4/AC-10).

The surface area and pore volume of prepared adsorbents were shown in Table S1. The order of surface area was followed as: Mn-Fe_3O_4/AC-1 (655 m^2 g^{-1})<Mn-Fe_3O_4/AC-5 (678 m^2 g^{-1})<AC (727 m^2 g^{-1})<Fe_3O_4/AC (800 m^2 g^{-1})<Mn-Fe_3O_4/AC-10 (819 m^2 g^{-1}). The carbon could react with iron oxides to produce carbon oxide, which resulted in the pore development and the improvement of surface area [20]. The surface area of Fe_3O_4/AC was increased from 727 m^2 g^{-1} to 800 m^2 g^{-1} compared to that of AC. When Mn was doped in Fe_3O_4/AC, the surface area was increased to 819 m^2 g^{-1} because Mn prevented the crystallization of iron oxides [21]. However, the amount of doping manganese further increased, and the surface area was decreased, which might be caused by the fact that excessive manganese could cause clogging of micropores and counteract the positive effect of iron oxide activation [11]. As known, the active sites were related to the specific surface area of the material [20], which could affect the adsorption capacity of the adsorbent for pollutants. The N_2 adsorption-desorption isotherm of Mn-Fe_3O_4/AC with the distinct adsorption and desorption branches was IV type (Fig. S3) [22], indicating that slit-shaped mesopores existed in the prepared materials [17,23]. Furthermore, total pore volumes of materials decreased with increasing the amount of metal

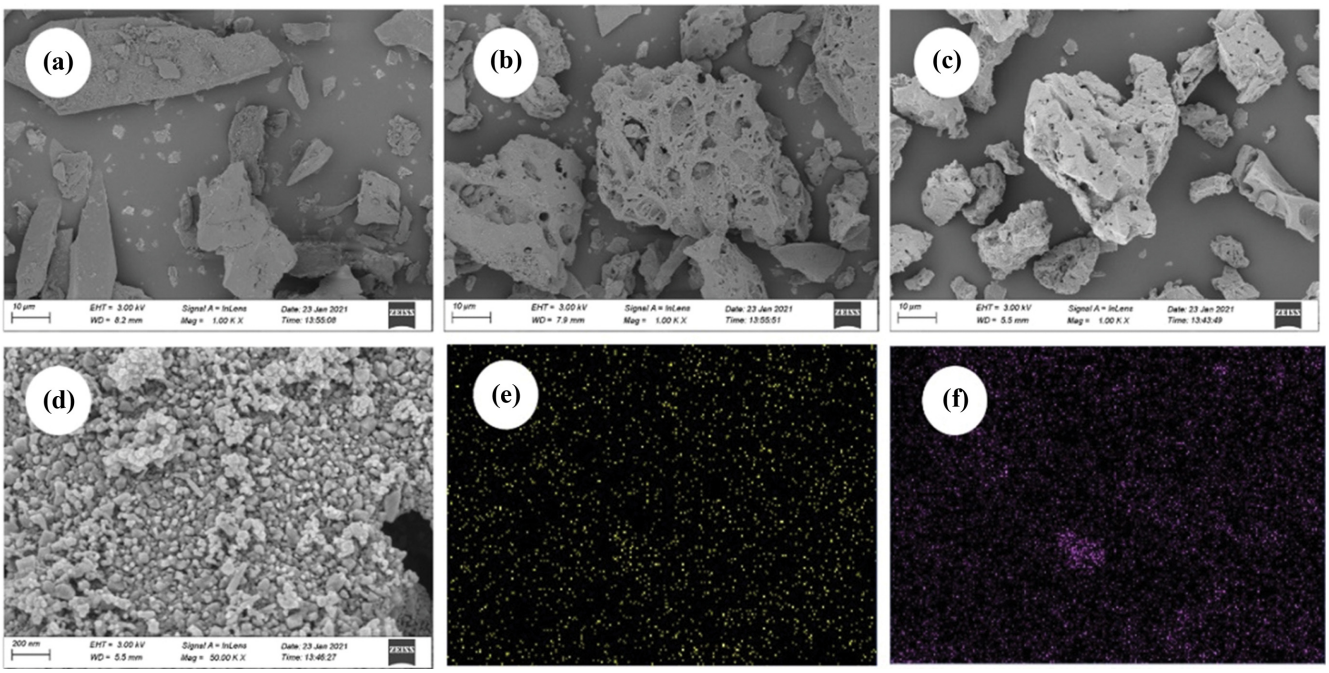

Fig. 1. SEM of (a) AC, (b) Fe_3O_4/AC, (c)-(d) Mn-Fe_3O_4/AC-10, (e) Mn and (f) Fe elemental mappings of Mn-Fe_3O_4/AC-10.

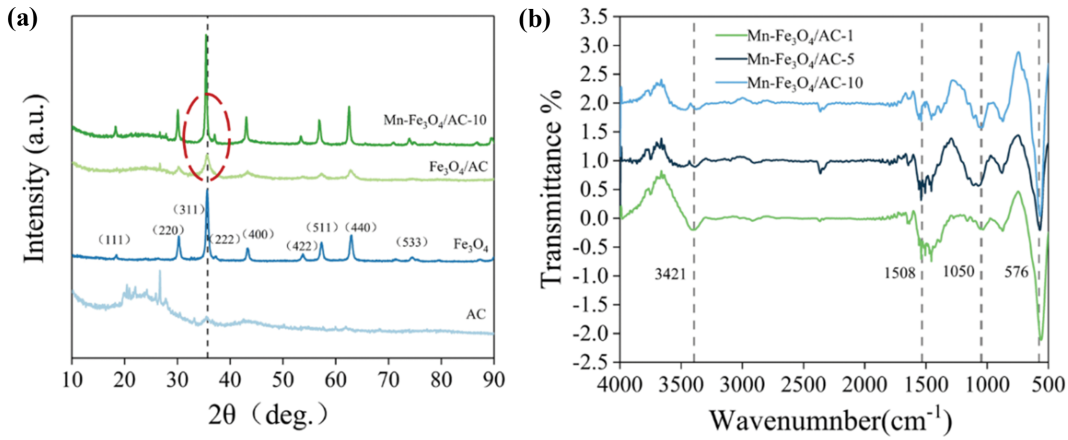

Fig. 2. (a) XRD patterns of Fe_3O_4, Fe_3O_4/AC, Mn-Fe_3O_4/AC-10 and AC, (b) FTIR spectra of Mn-Fe_3O_4/AC.

oxides (Mn and/or Fe), and the total pore volumes were 0.568, 0.559, 0.539, 0.446, and 0.403 $cm^3\ g^{-1}$ for the AC, Fe_3O_4/AC, Mn-Fe_3O_4/AC-10, Mn-Fe_3O_4/AC-5, Mn-Fe_3O_4/AC-1, respectively. The decrease in pore volume might be due to the filling of the prepared metal oxide particles in the pores [24,25].

The crystal phases of the prepared materials were detected by XRD, as shown in Fig. 2(a). As known, AC had a broad diffraction band with a typical graphite structure at 23° (002) [26]. The acidification process of AC could destroy the three-dimensional connection between carbon layers to form the graphene-like sheet skeleton, which could be conducive to the formation of AC pseudo-crystallinity (the peaks located from 14 to 26°) [26]. After the acidified AC was modified by Fe_3O_4, many new peaks appeared at 18.47°, 30.25°, 35.60°, 37.18°, 43.22°, 53.76°, 57.19°, 62.83°, and 74.47°, which correspond to the crystal plane (111), (220), (311), (222), (400), (422), (511), (440), and (533) of Fe_3O_4 (JCPDS 88-0315) [27]. According to Debye-Scherrer equation [28], the average lattice size of Fe_3O_4/AC sample was about 30.2 nm (2θ=35.60°). After doping Mn, the crystal plane (311) slightly shifted (Fig. S4), the position of diffraction peak shifted from 35.60° to 35.42°, and the lattice constant rose from 8.375 Å to 8.405 Å. The above analysis illustrated that the Mn had successfully been doped in Fe_3O_4/AC [29].

The functional groups on prepared materials were detected by FTIR (Fig. 2(b)). The broad absorption peaks at 3,421 cm^{-1} were attributed to the stretching vibration of -OH from adsorbed water. The peak at 1,508 cm^{-1} corresponded to C-C/C=C bonds, and the occurrence of peak at 1,050 cm^{-1} represented the bending vibration of hydroxyl group on metal oxides [30]. The characteristic absorption band of Mn-Fe_3O_4/AC spectrum at 576 cm^{-1} was caused by the stretching vibration of M-O bond (M=Fe and/or Mn) [31,32].

2. Adsorption Kinetics

The adsorption rate and adsorption equilibrium time can be

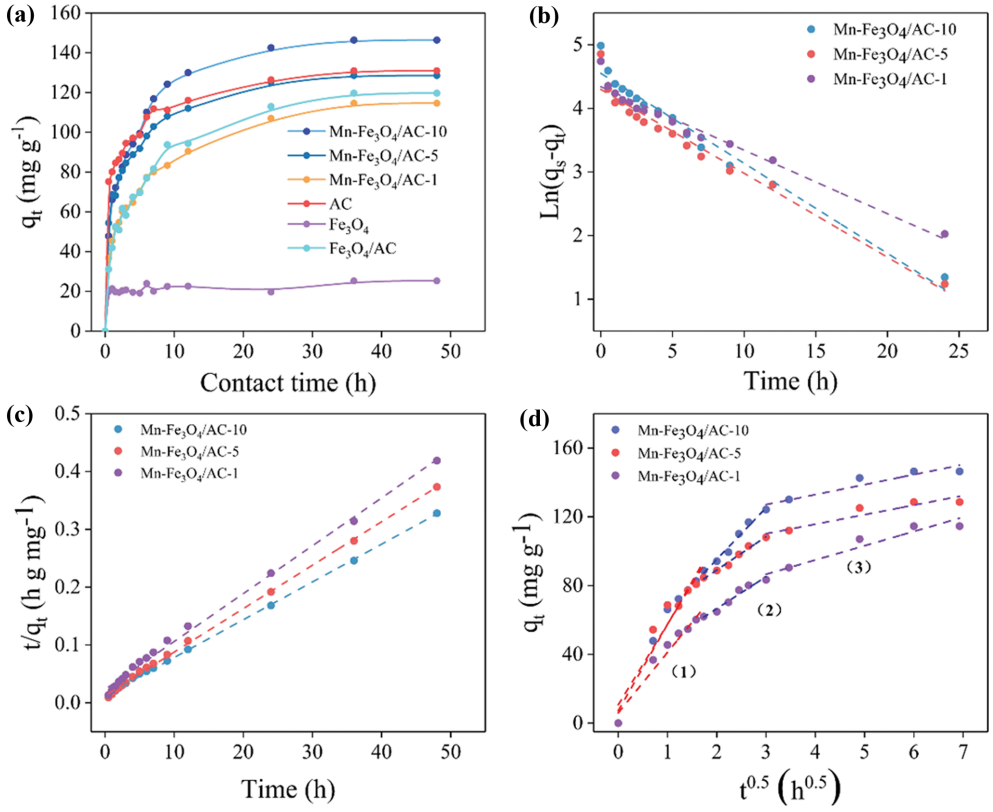

Fig. 3. (a) Time-dependent adsorption of SMZ onto adsorbent, adsorption kinetic models of (b) pseudo-first-order; (c) pseudo-second-order; and (d) intraparticle diffusion (Adsorption conditions: m/V=0.05 g L^{-1}, SMZ=10 mg L^{-1}, pH=6.1, t=48 h, T=298 K).

Table 1. The adsorption performance of different adsorbents for removal SMZ

Adsorbent	Conditions	Maximum adsorption capacity (mg g^{-1})	Ref.
Core-shell MIP	Adsorbent: 2 g L^{-1}, adsorbate: 0.3 mM, 308 K	8.10	[43]
Multi-walled carbon nanotubes	Adsorbent: 0.2 g L^{-1}, adsorbate: 20 mg L^{-1}, pH=5, 298 K	38.1	[35]
Mesoporous cellulose biochar	Adsorbent:1 g L^{-1}, adsorbate: 50 mg L^{-1}, pH=6.4, 298 K	86.8	[36]
Magnetic COFs	Adsorbent: 0.11 g L^{-1}, adsorbate: 100 mg L^{-1}, 298 K	113	[37]
TPB-DMTP-COF	Adsorbent: 0.1 g L^{-1}, adsorbate: 40 mg L^{-1}, pH=6, 298 K	209	[38]
Mn-Fe$_3$O$_4$/AC-1:10	Adsorbent: 0.05 g L^{-1}, adsorbate: 10 mg L^{-1}, pH=6.1, 298 K	308	This work

obtained from adsorption kinetic curve. In addition, kinetic models can illustrate the mechanism of pollutants' adsorption. As shown in Fig. 3(a), the adsorption rates except for Fe_3O_4 increased sharply within 9 h, then flattened from 9 to 36 h. Finally, the adsorption process reached equilibrium at 48 h. The high adsorption rate of SMZ at the beginning of adsorption process was related to the high concentration of adsorbate and the effective adsorption sites of adsorbent [33]. The adsorption capacities were followed as: Mn-Fe_3O_4/AC-10 (146 mg g^{-1})>Mn-Fe_3O_4/AC-5 (129 mg g^{-1})>Mn-Fe_3O_4/AC-1 (120 mg g^{-1}), because the surface area of Mn-Fe_3O_4/AC-10 was larger than that of the others, which could provide more adsorption sites. While the surface area of Mn-Fe_3O_4/AC-5 (678 m^2 g^{-1}) was similar to that of Mn-Fe_3O_4/AC-5 (655 m^2 g^{-1}), the adsorption capacity of Mn-Fe_3O_4/AC-5 (129 mg g^{-1}) was larger than that of the Mn-Fe_3O_4/AC-1 (120 mg g^{-1}), which might be caused by the total pore volumes. Olivares-Marín et al. reported that the larger pore volume was conducive to the adsorption of pollutants [34]. Therefore, the best adsorption capacity was Mn-Fe_3O_4/AC-10, and then Mn-Fe_3O_4/AC-5.

An overview of published works on SMZ removal based on different adsorbents as well as ours in this work was shown in Table 1. Among adsorbents, the maximum adsorption capacities of SMZ using core-shell MIP, multi-walled carbon nanotubes, mesoporous cellulose biochar, magnetic COFs, and TPB-DMTP-COF were about 8.10, 38.1, 86.8, 113, and 209 mg g^{-1}, respectively [35-38]. In this study, the maximum adsorption capacity of Mn-Fe_3O_4/AC-10 was about 308 mg g^{-1}. In comparison, the maximum adsorption capacity of the present adsorbent is higher than that of other adsorbents, and the preparation process of Mn-Fe_3O_4/AC was simple and cheap (co-precipitation method). When compared with these reported works, the Mn-Fe_3O_4/AC might be potentially used in environmental purification.

To further investigate the detailed information about the adsorption process, pseudo-first-order (PFO), pseudo-second-order (PSO), and intraparticle diffusion (ID) models rate equations were employed, and the equations were shown in Text S1. The kinetic parameters and correlation coefficient (R^2) were displayed in Table 2. The R^2 of the pseudo-second-order kinetics model was much higher

Table 2. Kinetic parameters based on the pseudo-first, pseudo-second order and intraparticle diffusion models for SMZ removal

Kinetic model	Adsorbent		
	Mn-Fe_3O_4/AC-10	Mn-Fe_3O_4/AC-5	Mn-Fe_3O_4/AC-1
Pseudo-first-order			
k_1 (h^{-1})	0.142	0.0999	0.132
$q_{e.cal}$ (mg g^{-1})	94.7	76.7	73.6
R^2	0.969	0.959	0.956
Pseudo-second-order			
k_2 (g mg^{-1} h^{-1})	0.00330	0.00449	0.00697
$q_{e.cal}$ (mg g^{-1})	153	13	97.6
R^2	0.999	0.999	0.995
Intraparticle diffusion			
k_{d1} (mg g^{-1} h^{-1})	50.1	46.9	35.2
k_{d2} (mg g^{-1} h^{-1})	36.5	22.5	24.8
k_{d3} (mg g^{-1} h^{-1})	5.82	5.55	8.31
C_1	7.28	10.7	5.96
C_2	20.0	42.9	15.4
C_3	110	42.9	61.6
$(R_1)^2$	0.961	0.917	0.954
$(R_2)^2$	0.979	0.976	0.982
$(R_3)^2$	0.894	0.899	0.926

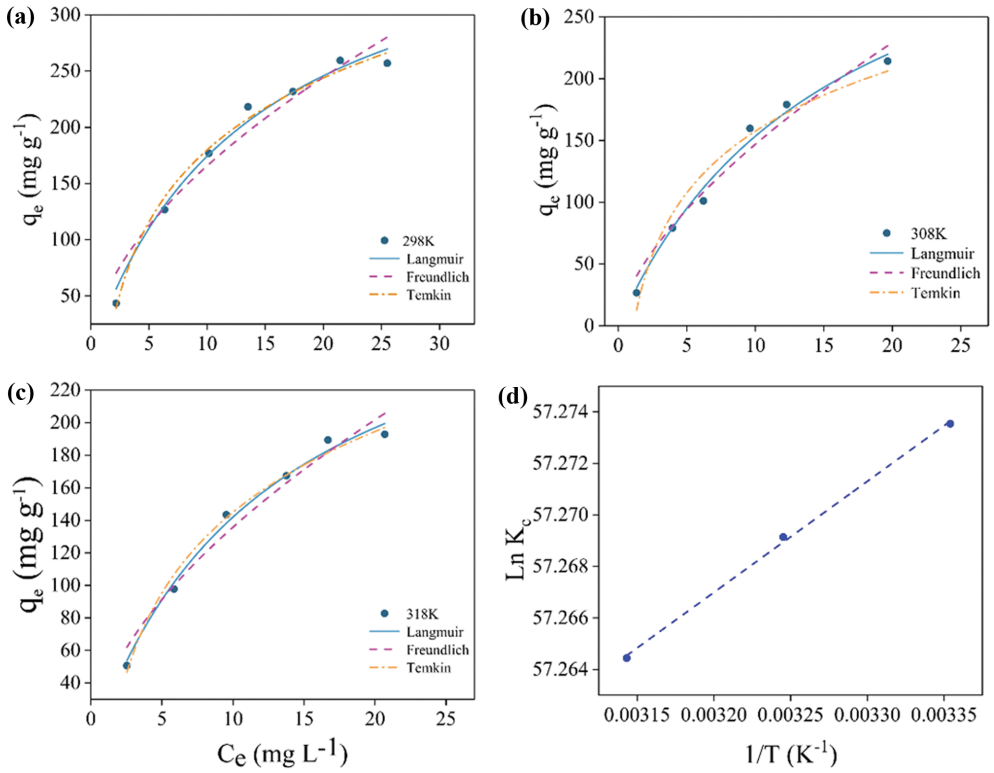

Fig. 4. Comparison of equilibrium experimental data with the Langmuir, Freundlich and Temkin models at (a) 298 K, (b) 308 K and (c) 318 K (d) Linear plots of lnK_c versus 1/T for the adsorption of SMZ. Adsorption conditions: m/V=0.05 g L^{-1}, SMZ=10 mg L^{-1}, pH=6.1, t=48 h, shaking speed 120 rpm.

than that of the pseudo-first-order kinetics model (Fig. 3(b) and (c)). At the same time, the maximum adsorption capacity ($q_{s,max}$) values also approached the experimental data, indicating that physical adsorption was most likely to be the control step of the adsorption process [39]. The intraparticle diffusion model could well explain the rate-limiting mechanism. As shown in Fig. 3(d), diffusion-controlled adsorption process could be divided into three linear parts, which indicated that the process was controlled by two or more simultaneous mechanisms [40,41]. In the first sharp slope stage, the SMZ molecular quickly bound to the active sites on the surface Mn-Fe_3O_4/AC. In the second stage, when the surface active sites were quickly occupied, the SMZ molecules continued to bind to active sites inside the Mn-Fe_3O_4/AC, which caused the adsorption rate to decrease. And in the last stage, the SMZ molecules relied on intraparticle diffusion binding to the remaining small number of active sites, which needed to overcome molecular diffusion resistance [39,42].

3. Adsorption Isotherms and Thermodynamics

Isothermal adsorption was used to describe the distribution characteristics of adsorbates and understand the process of adsorption. The isotherm models, including Langmuir, Freundlich, and Temkin isotherm, were employed, and their description was shown in Text S2. Fig. 4 showed the isotherms of Mn-Fe_3O_4/AC-10 at different temperatures. According to the comparison of the regression coefficient R^2 (Table 3), the adsorption process fitted well the Langmuir isotherm model, indicating that the adsorption of Mn-Fe_3O_4/AC-10 to SMZ was monolayer adsorption. In addition, the adsorption process was favorable because of the R_L=0.58. According to thermodynamic analysis of Langmuir isotherm model, the $q_{s,max}$ could reach 380 mg g^{-1} at 298 K.

According to the adsorption isotherm, thermodynamic parameters including Gibbs free energy (ΔG kJ mol^{-1}), enthalpy change (ΔH, kJ mol^{-1}), and entropy change (ΔS, kJ $kmol^{-1}$ K^{-1}) could be calculated via Eqs. (4-6) [44]. And the thermodynamic parameters were shown in Table 4.

$$K_d = \frac{V(C_0 - C_e)}{mC_e} \quad (4)$$

Table 3. Isotherm parameters for SMZ adsorbed onto Mn-Fe_3O_4/AC-10

Type	Temperature (K)		
	298	308	318
Langmuir isotherm			
q_{max} (mg g^{-1})	380	348	297
K_L (L mg^{-1})	0.0718	0.0629	0.0792
R^2	0.985	0.988	0.991
Freundlich isotherm			
K_F ((mg g^{-1})(L mg^{-1})$^{1/n}$)	45.6	33.5	36.4
n	1.78	1.56	1.75
R^2	0.949	0.967	0.968
Temkin isotherm			
B (J mol^{-1})	92.4	71.9	71.6
K_T (L g^{-1})	0.701	0.894	0.758
R^2	0.988	0.961	0.989

Table 4. Thermodynamic parameters for SMZ adsorbed onto Mn-Fe_3O_4/AC-10

T (K)	ΔG (kJ mol^{-1})	ΔH (kJ mol^{-1})	ΔS (kJ $kmol^{-1}$ K^{-1})	LnK_c
298	−142	0.359	0.475	57.3
308	−147			57.3
318	−152			57.3

$$\Delta G = -RTLnK_c \quad (5)$$

$$LnK_c = \frac{\Delta S}{R} - \frac{\Delta H}{RT} \quad (6)$$

where K_d is the distribution coefficient, R is molar gas constant (8.314 J mol^{-1} K^{-1}), K_c is the equilibrium constant, and LnK_c can be calculated by plotting LnK_d versus C_e and extrapolating C_e to 0 [45], and the linear graph between 1/T and LnK_c is shown in Fig. 4(d).

The ΔG value was negative, which confirmed that adsorption was spontaneous. The ΔS value was greater than zero, which was conducive to the rapid diffusion of SMZ molecules to the adsorbent, and also explained the random and disorderly increase of the adsorbent-adsorbent interface [46]. The value of ΔH was negative, indicating that the adsorption was exothermic. The reason might be that the temperature rise caused the bond energy between the adsorbate and the active site on the surface of the adsorbent to weaken [47], and it also indicated that the adsorption process was chemical adsorption [48].

4. Adsorption Mechanism

As known, the pH of solution could affect the present state of the adsorbate and the surface charge of the adsorbent [49]. SMZ possessed amine (-NH_2) and amide groups (-NH-) with the pK_{a1} of 2.06 and pK_{a2} of 6.90, respectively [50]. From Fig. 5(a), when pH of solutions was <2.06, 2.06-6.90, and >6.90, the SMZ molecules would mainly exist in the form of SMZ^+, SMZ^0, and SMZ^-, respectively [38]. According to zeta potential analysis, the pH_{PZC} of Mn-Fe_3O_4/AC was about 5.27, and the surface charge of Mn-Fe_3O_4/AC was positive at pH<pH_{PZC}; otherwise, it was negative. When the pH of solution was 2-6, the surface charge of the adsorbent gradually changed from positive to negative, while the main existing states of SMZ molecules changed from SMZ^+ to SMZ^0. Furthermore, when the pH of solution continued to increase, the surface charge of Mn-Fe_3O_4/AC became more negative, and the SMZ^- mainly existed in the solution, which led to reducing the removal efficiency of SMZ via electrostatic repulsion. However, the removal efficiency of SMZ was almost unchanged within this range pH solution, revealing the effect of electrostatic force between SMZ molecules and adsorbent was unobvious, and the adsorption process might be dominated by other forces. Previous studies had found that π^+-π electron donor-acceptors (EDA) were generated via interaction between the protonated aniline ring (π electron acceptor) caused by the high electronegativity of the -NH_3^+ and -SO_2NH- groups of SMZ^+ and the C-C and C=C groups (π electron donor) on the surface of adsorbents (i.e., biochars [20] and black carbon [51]). As shown in Fig. 5(b), the C 1s spectra of Mn-Fe_3O_4/AC-10 before and after adsorption could be deconvoluted

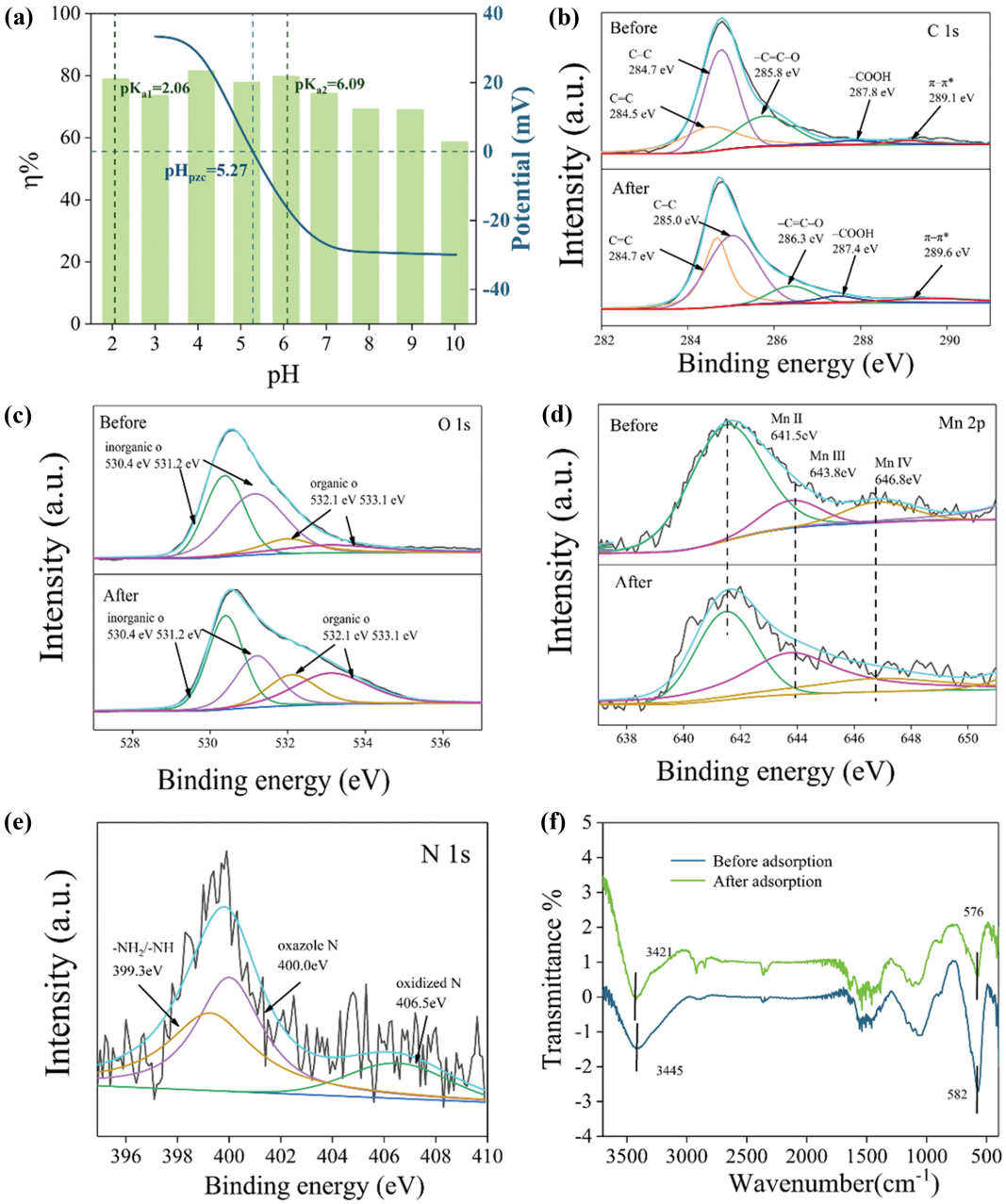

Fig. 5. Effect of (a) pH; (b) The high-resolution C 1s spectra, (c) The high-resolution O 1s spectra, (d) The high-resolution Mn 2p spectra, (e) The high-resolution N1s spectrum of Mn-Fe_3O_4/AC-10; (f) FTIR spectra of SMZ before and after adsorption.

into five different peaks at 284.5-284.7, 284.7-285.0, 285.8-286.3, 287.8-287.4, and 289.1-289.6 eV, which correspond to C=C, C-C, -C=CO, -COOH, and π-π* satellite, respectively [52]. The contents of C=C peak increased from 25.2% to 31.7% after adsorption, indicating that there was π^+-π EDA in the mode of interaction between SMZ and Mn-Fe_3O_4/AC-10. Except for π^+-π EDA, the hydrogen bond between the -NH_2 and -NH- groups of SMZ and oxygen-containing functional groups of Mn-Fe_3O_4/AC might be considered the other driving force [53]. As shown in O 1s (Fig. 5(c)), peaks at 532.1 and 533.2 eV were attributed to organic O (i.e., C=O, C-OH, and -COOH), and peaks at 530.4 and 532.2 eV to inorganic O (i.e., Fe and Mn oxides) [12]. The content of organic O increased from 23.2% to 41.7% after SMZ adsorption, suggesting that these groups participated in adsorption via hydrogen bonds [9,54]. And the -OH peak of the FTIR spectra (Fig. 5(f)) of Mn-Fe_3O_4/AC shifted from 3,421 to 3,445 cm^{-1} after adsorption, which could also confirm the existence of hydrogen bond interaction between Mn-Fe_3O_4/AC-10 and SMZ [55].

Interestingly, the valence states of Mn in the Mn-Fe_3O_4/AC changed before and after adsorption. As shown in the high-resolution Mn 2p spectra (Fig. 5(d)), the binding energies of Mn 2p for Mn(II), Mn(III), and Mn(IV) were located at 641.5, 643.8, and 646.8 eV, respectively [13]. Positions of Mn had no obvious shift before and after SMZ adsorption. However, the content of Mn(II)

decreased from 74.2% to 53.5%, and the content of Mn(IV) decreased from 12.2% to 7.8%, indicating that Mn participated in the redox reaction. Obviously, the N 1s spectrum of the newly appeared element after the adsorption of SMZ showed that there was also the presence of oxidized N beside the -NH_2/-NH- and oxazole N of SMZ (Fig. 5(e)) [9], which further affirmed that the redox reaction occurred between Mn-Fe_3O_4/AC-10 and SMZ with -NH_2 and -NH- having strong reducing activity. And the peak of M-O at 576 cm^{-1} of Mn-Fe_3O_4/AC-10 showed a clear shift to 582 cm^{-1} in FTIR (Fig. 5(f)), which also indirectly explained that the redox reaction occurred during the adsorption process [56]. Based on the above analysis, the removal of SMZ by Mn-Fe_3O_4/AC-10 not only included adsorption via electrostatic interactions, π^{+}-π EDA interactions, and hydrogen bonds, but also had redox reaction.

5. Reusability and Regeneration

The reusability of adsorbent was considered to be a crucial factor for sustainable application. After each adsorption, the adsorbent was put into 0.5 mol L^{-1} NaOH solution for desorption, and then dried and the above conditions were repeated for adsorption. As shown in Fig. S5, after five cycles of adsorption process, the adsorption capacity was still high (146, 144, 137, 128, 125, and 121 mg g^{-1}, respectively), indicating the material had excellent reusability. However, the adsorption capacity was slightly reduced compared to that of the raw Mn-Fe_3O_4/AC. The SMZ in the pores of Mn-Fe_3O_4/AC could not be completely desorbed, and they still occupied a certain quantity of adsorption sites, which led to a gradual weakening of the adsorption capacity with the increase of the number of cycles. To achieve the regeneration of the Mn-Fe_3O_4/AC, the desorption time of the sorbent in NaOH solution was extended or Mn-Fe_3O_4/AC was treated with ozone for direct oxidative removal of SMZ on the Mn-Fe_3O_4/AC.

CONCLUSION

Mn-Fe_3O_4/AC was successfully fabricated using a simple, facile and environmentally friendly strategy. When atom proportion of Fe/Mn was 11.2 for the Mn-Fe_3O_4/AC, it exhibited excellent adsorption capacity for SMZ from aqueous solution (146 mg g^{-1}) compared with other atom proportions of Fe/Mn (1 : 5 and 1 : 1), due to its biggest specific surface area (819 m^2 g^{-1}), which could provide more adsorption sites for the adsorption of SMZ. Furthermore, the adsorption capacity of Mn-Fe_3O_4/AC was evidently higher than some recently reported results. The efficient adsorption was mainly attributed to hydrogen bonds, π^{+}-π and electrostatic interactions between SMZ and Mn-Fe_3O_4/AC. In addition, the part of SMZ could be degraded via redox reactions. The adsorption process followed the pseudo-second-order kinetic model and Langmuir model. After six cycles of adsorption-desorption experiments, the adsorption capacity of Mn-Fe_3O_4/AC for SMZ was still high (146, 144, 137, 128, 125, and 121 mg g^{-1}, respectively), indicating the effective recovery performance of Mn-Fe_3O_4/AC in practical application.

ACKNOWLEDGEMENTS

Financial support from the Hunan Provincial Key Research and Development Program (2022SK2068) is acknowledged.

NOTES

The authors declare no competing financial interests.

CREDIT AUTHORSHIP CONTRIBUTION STATEMENT

Wenxiu Zhu and **Xinghao Liu:** Investigation, Data curation, Writing-original draft. **Haipu Li:** Writing review & editing. **Haipu Li** and **Zhaoguang Yang:** Conceptualization, Supervision, Project administration.

SUPPORTING INFORMATION

Additional information as noted in the text. This information is available via the Internet at http://www.springer.com/chemistry/journal/11814.

REFERENCES

1. M. Qiao, G. G. Ying, A. C. Singer and Y. G. Zhu, *Environ. Int.*, **110**, 160 (2018).
2. M. Rysz and P. J. Alvarez, *Water Res.*, **38**, 3705 (2004).
3. X. Zhuang, X. Li, Y. Yang, N. Wang, Y. Shang, Z. Zhou, J. Li and H. Wang, *Water*, **12**, 2273 (2020).
4. L. Zhang and S. Shen, *J. Ind. Eng. Chem.*, **83**, 123 (2020).
5. S. Errayess, A. Lahcen, L. Idrissi, C. Marcoaldi, S. Chiavarini and A. Amine, *Spectrochim. Acta. A*, **181**, 276 (2017).
6. Y. Liu, X. Liu, W. Dong, L. Zhang, Q. Kong and W. Wang, *Sci. Rep.*, **7**, 12437 (2017).
7. A. Asfaram, M. Ghaedi, A. Goudarzi and M. Rajabi, *Dalton. Trans.*, **44**, 14707 (2015).
8. P. Yu, X. Li, X. Zhang, H. Zhou, Y. Xu, Y. Sun and H. Zheng, *Sep. Purif. Technol.*, **254**, 117662 (2021).
9. M. Lv, D. Li, Z. Zhang, B. E. Logan, G. Liu, M. Sun, C. Dai and Y. Feng, *Sci. Total. Environ.*, **757**, 143717 (2021).
10. H. Yu, J. Yang, P. Shi, M. Li and J. Bian, *ACS. Omega*, **6**, 16837 (2021).
11. J. Alvarez-Cruz and S. Garrido-Hoyos, *Sci. Total Environ.*, **668**, 47 (2019).
12. J. Guo, C. Yan, Z. Luo, H. Fang, S. Hu and Y. Cao, *J. Environ. Sci.* (China), **85**, 168 (2019).
13. H. Zhou and G. Xu, *Sci. Total Environ.*, **708**, 134422 (2020).
14. J. Liang, Y. Fang, Y. Luo, G. Zeng, J. Deng, X. Tan, N. Tang, X. Li, X. He, C. Feng and S. Ye, *Environ. Sci. Pollut. Res.*, **26**, 5892 (2019).
15. C. Kim, Z. Zhang, L. Wang, T. Sun and X. Hu, *J. Taiwan Inst. Chem.*, **67**, 418 (2016).
16. X. Du, Q. Han, J. Li and H. Li, *J. Taiwan Inst. Chem.*, **76**, 167 (2017).
17. K. Lu, T. Wang, L. Zhai, W. Wu, S. Dong, S. Gao and L. Mao, *J. Colloid Interface Sci.*, **539**, 553 (2019).
18. H. Zhang, Y. He, L. Lai, G. Yao and B. Lai, *Sep. Purif. Technol.*, **245**, 116449 (2020).
19. Y. Huang, W. Xu, L. Hu, J. Zeng, C. He, X. Tan, Z. He, Q. Zhang and D. Shu, *Catal. Today*, **297**, 143 (2017).
20. S. Zeng, Y. K. Choi and E. Kan, *Sci. Total. Environ.*, **750**, 141691

(2021).
21. W. Xie and D. Zhao, *Sci. Total Environ.*, **542**, 1020 (2016).
22. J. Li, L. Wang, Y. Ren, Y. Zhang, Y. Wang, A. Hu and X. He, *Ionics*, **22**, 167 (2015).
23. A. Baye, R. Appiah-Ntiamoah and H. Kim, *Sci. Total Environ.*, **712**, 135492 (2020).
24. J. Zhang, S. Qu, L. Li, P. Wang, X. Li, Y. Che and X. Li, *J. Chem. Eng. Data*, **63**, 1737 (2018).
25. X. Zhang, L. Zhang, Y. Liu, M. Li, X. Wu, T. Jiang, C. Chen and Y. Peng, *Environ. Pollut.*, **262**, 114184 (2020).
26. R. Ramos, A. Biz, D. Tavares, M. Kolicheski and T. Dantas, *Soil, Air, Water*, **48**, 190043 (2020).
27. X. Wang, Y. Zhang, R. Shan and H. Hu, *Ceram. Int.*, **47**, 3219 (2021).
28. A. Sharma, Z. Siddiqi and D. Pathania, *J. Mol. Liq.*, **240**, 361 (2017).
29. Z. Chen, Y. Zheng, Y. Liu, W. Zhang, Y. Wang, X. Guo, X. Tang, Y. Zhang, Z. Wang and T. Zhang, *Mater. Chem. Phys.*, **238**, 121893 (2019).
30. W. Zhang, W. Liu, G. Li, W. Du, J. Lu, J. Song, Q. Yang, X. Li, H. Xu, X. He and J. Ma, *Chem. Eng. J.*, **407**, 127142 (2021).
31. P. Nazari, N. Askari and S. Rahman Setayesh, *Chem. Eng. Commun.*, **207**, 665 (2019).
32. M. M-Ridha, Y. Hasan and M. Ibrahim, *Sep. Sci. Technol.*, **56**, 2721 (2020).
33. A. Alqadami, M. Naushad, M. Abdalla, T. Ahamad, Z. Abdullah Alothman, S. Alshehri and A. Ghfar, *J. Clean. Prod.*, **156**, 426 (2017).
34. M. Olivares-Marín, V. Del Prete, E. Garcia-Moruno, C. Fernández-González, A. Macías-García and V. Gómez-Serrano, *Food Control*, **20**, 298 (2009).
35. Q. Yang, G. Chen, J. Zhang and H. Li, *RSC Adv.*, **5**, 25541 (2015).
36. Q. Chen, J. Zheng, J. Xu, Z. Dang and L. Zhang, *Chem. Eng. J.*, **356**, 341 (2019).
37. S. Zhuang, R. Chen, Y. Liu and J. Wang, *J. Hazard. Mater.*, **385**, 121596 (2020).
38. S. Zhuang, Y. Liu and J. Wang, *J. Hazard. Mater.*, **383**, 121126 (2020).
39. T. Saleh, *J. Clean. Prod.*, **172**, 2123 (2018).
40. H. Tran, S. You and H. Chao, *J. Environ. Manage.*, **188**, 322 (2017).
41. X. Liu, S. Hu, D. Xu and D. Shao, *Korean J. Chem. Eng.*, **37**, 776 (2020).
42. Y. Shi, X. Kong, C. Zhang, Y. Chen and Y. Hua, *Chem. Eng. J.*, **215**, 113 (2013).
43. W. Huang, Y. Qing, N. Wang, Y. Lu, T. Liu, T. Liu, W. Yang and S. Li, *Mater.*, **11**, 2067 (2018).
44. X. Liu, C. Cheng, C. Xiao, D. Shao, Z. Xu, J. Wang, S. Hu, X. Li and W. Wang, *Appl. Surf. Sci.*, **411**, 331 (2017).
45. R. Hu, X. Wang, S. Dai, D. Shao, T. Hayat and A. Alsaedi, *Chem. Eng. J.*, **260**, 469 (2015).
46. H. Aghdasinia and H. R. Asiabi, *Environ. Earth. Sci.*, **77**, 218 (2018).
47. A. Jawad, Y. Ngoh and K. Radzun, *J. Taibah University Sci.*, **12**, 371 (2018).
48. S. Subramani and N. Thinakaran, *Process. Saf. Environ.*, **106**, 1 (2017).
49. L. Mouni, L. Belkhiri, J.-C. Bollinger, A. Bouzaza, A. Assadi, A. Tirri, F. Dahmoune, K. Madani and H. Remini, *Appl. Clay. Sci.*, **153**, 38 (2018).
50. R. Liu, Q. Yan, Y. Tang, R. Liu, L. Huang and Q. Shuai, *J. Hazard. Mater.*, **421**, 126702 (2022).
51. M. Teixido, J. Pignatello, J. Beltran, M. Granados and J. Peccia, *Environ. Sci. Technol.*, **45**, 10020 (2011)
52. Y. Lan, T. Chen, H. Tsai, H. Wu, J. Lin, I. Lin, J. Lee and C. Chen, *Langmuir*, **32**, 9530 (2016).
53. X. Guo, Y. Yin, C. Yang and Q. Zhang, *Chem. Intermediat.*, **42**, 6423 (2016).
54. J. Wang, H. Tao, T. Lu and Y. Wu, *J. Colloid Interface Sci.*, **584**, 114 (2021).
55. H. Tran, Y. Wang, S. You and H. Chao, *Process. Saf. Environ.*, **107**, 168 (2017).
56. X. Liu, M. Gao, W. Qiu, Z. H. Khan, N. Liu, L. Lin and Z. Song, *Environ. Sci. Pollut. Res.*, **26**, 17373 (2019).

Supporting Information

Synthesis of manganese-iron oxides/activated carbon as a highly effective adsorbent for sulfamerazine pollutant removal

Wenxiu Zhu*,,‡, Xinghao Liu*,**,‡, Zhaoguang Yang*,**,†, and Haipu Li*,**,†**

*Center for Environment and Water Resource, College of Chemistry and Chemical Engineering, Central South University, Changsha 410083, P. R. China
**Key Laboratory of Hunan Province for Water Environment and Agriculture Product Safety, Changsha 410083, P. R. China
(*Received 19 January 2022 • Revised 28 March 2022 • Accepted 14 April 2022*)

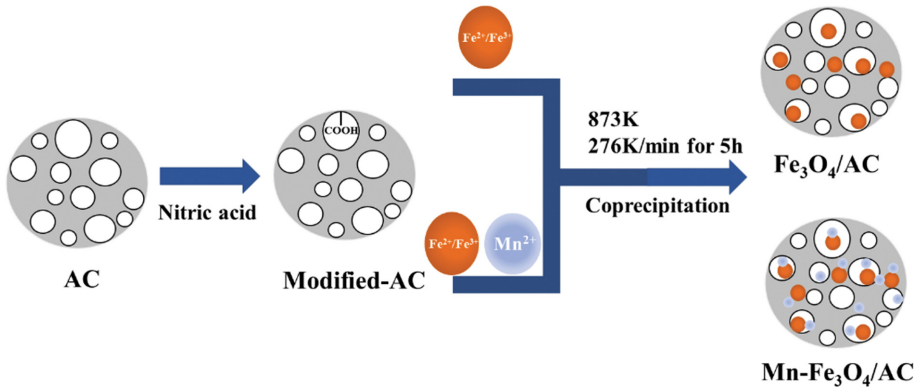

Fig. S1. Preparation process of Fe_3O_4/AC and Mn-Fe_3O_4/AC.

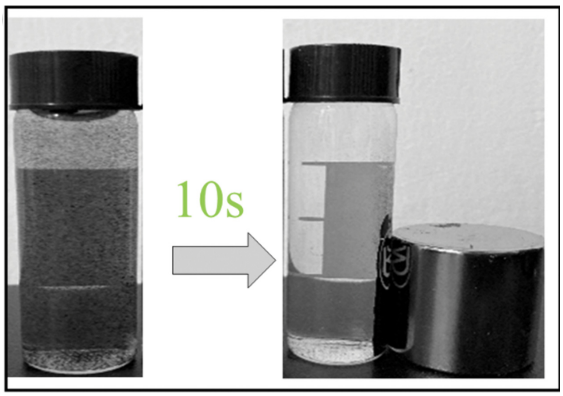

Fig. S2. Separation of the Mn-Fe_3O_4/AC-10 from solution via magnet.

Text S1

The equations of pseudo first-order (PFO), pseudo second-order (PSO) and intraparticle diffusion (ID) models were shown in S1-S3 [1]:

$$\text{PFO: } \ln(q_e - q_t) = \ln q_e - k_1 t \quad \text{(S1)}$$

$$\text{PSO: } \frac{t}{q_t} = \frac{1}{k_2 q_e^2} + \frac{1}{q_e} t \quad \text{(S2)}$$

$$\text{ID: } q_t = k_{di} t^{0.5} + C_i \quad \text{(S3)}$$

where k_1 (h^{-1}), k_2 (g mg^{-1} h^{-1}) and k_i (mg g^{-1} $h^{-0.5}$) are the first-order, second-order and intraparticle diffusion rate constant adsorption, C_i (mg g^{-1}) is the boundary layer effect constant. The k_{di} and C_i parameters can be obtained by plotting the slope and inter-

Table S1. Specific surface areas and pore sizes of AC, Fe_3O_4/AC, Mn-Fe_3O_4/AC-10, Mn-Fe_3O_4/AC-5 and Mn-Fe_3O_4/AC-1

Sample	BET surface area (m^2 g^{-1})	Total pore volume (cm^3 g^{-1})	Micropore volume (cm^3 g^{-1})	Mesopore volume (cm^3 g^{-1})
AC	727	0.568	0.150	0.417
Fe_3O_4/AC	800	0.559	0.199	0.360
Mn-Fe_3O_4/AC-10	819	0.539	0.209	0.331
Mn-Fe_3O_4/AC-5	678	0.446	0.171	0.275
Mn-Fe_3O_4/AC-1	655	0.403	0.166	0.237

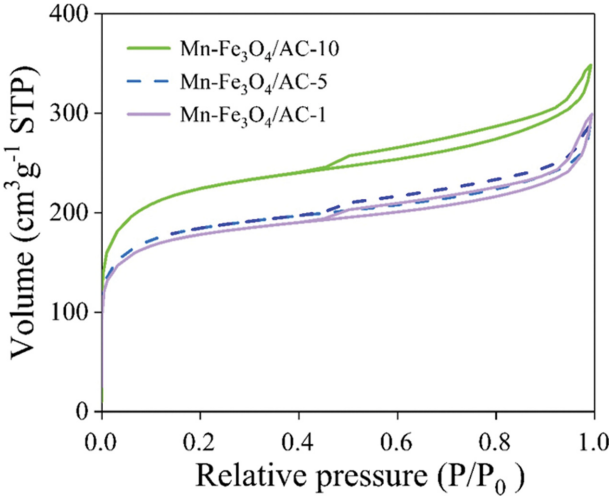

Fig. S3. The N_2 adsorption-desorption isotherms of Mn-Fe_3O_4/AC-10, Mn-Fe_3O_4/AC-5 and Mn-Fe_3O_4/AC-1.

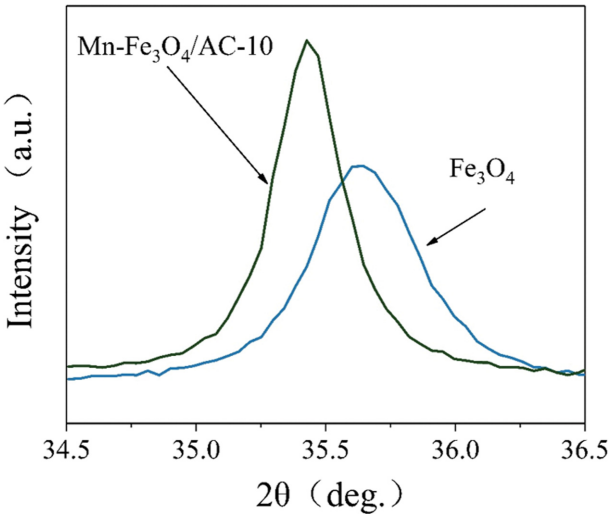

Fig. S4. XRD patterns of Mn-Fe_3O_4/AC-10 and Fe_3O_4.

cept of the equation by C_t versus $t^{0.5}$. The C_i value increases with the thickness of the boundary layer [2].

Text S2

The Langmuir adsorption model often assume that the adsorption process is uniform and the monomolecular layer adsorption [3]. The Langmuir nonlinear isotherm equation is showed by Eq. (S4). In addition, the separation factor (R_L, Eq. S5) is defined as a dimensionless object in the Langmuir nonlinear isotherm equation, which can judge that whether the adsorption reaction is a favorable process [4].

$$q_e = \frac{q_{max} K_L C_e}{1 + K_L C_e} \quad (S4)$$

$$R_L = \frac{1}{1 + K_L C_0} \quad (S5)$$

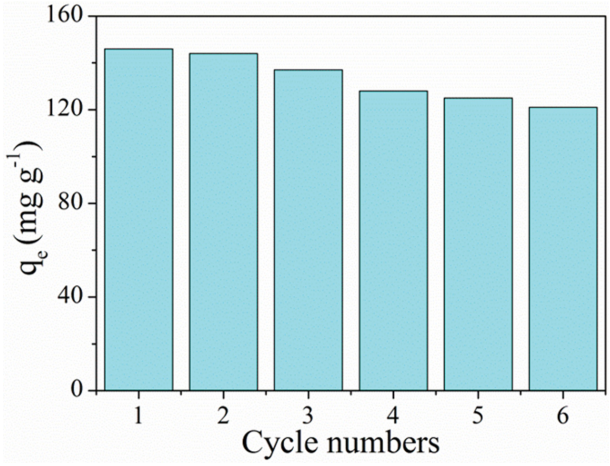

Fig. S5. Reusability for SMZ adsorbed onto Mn-Fe_3O_4/AC-10.

where the q_{max} (mg g^{-1}) is the maximum adsorption capacity; C_e is the concentration of SMZ in the solution; K_L (L mg^{-1}) is the binding constant. When R_L>1, adsorption process is adverse adsorption; when R_L=1, adsorption process is linear adsorption; when R_L=0, adsorption process is irreversible adsorption; at last, when 1>R_L>0, adsorption process is favorable adsorption.

The Freundlich adsorption model is empirical formula, suitable for non-uniform surface adsorption. The Freundlich isotherm equation is displayed Eq. (S6) [5].

$$q_e = K_F C_e^{1/n} \quad (S6)$$

where the K_F and n are the constant related to adsorption capacity and adsorption strength.

The Temkin isotherm assumes the linear relationship between the heat of adsorption and the temperature, and the isothermal constant increases with the increase of the adsorption temperature. It is displayed Eq. (S7) [1].

$$q_e = B\mathrm{Ln}K_T + B\mathrm{Ln}C_e \quad (S7)$$

where B (J mol^{-1}) is the gas constant; K_T (L g^{-1}) is the constant related to the heat of adsorption.

REFERENCES

1. W. Konicki, M. Aleksandrzak, D. Moszynski and E. Mijowska, *J. Colloid Interface Sci.*, **496**, 188 (2017).
2. G. Adebisi, Z. Chowdhury and P. Alaba, *J. Cleaner Prod.*, **148**, 958 (2017).
3. Z. Movasaghi, B. Yan and C. Niu, *Ind. Crops Prod.*, **127**, 237 (2019).
4. L. Lim, N. Priyantha, D. Tennakoon, H. Chieng, M. Dahri and M. Suklueng, *Arabian J. Chem.*, **10**, S3216 (2017).
5. M. Zubair, N. Jarrah, M. Manzar, M. Al-Harthi, M. Daud, N. Mu'azu and S. Haladu, *J. Mol. Liq.*, **230**, 344 (2017).